# On Multifractal Tissue Characterization in Ultrasound Imaging

Edouard Villain, Herwig Wendt, Adrian Basarab, Denis Kouamé

# ON MULTIFRACTAL TISSUE CHARACTERIZATION IN ULTRASOUND IMAGING

*Edouard Villain, Herwig Wendt, Adrian Basarab, Denis Kouamé*

IRIT, CNRS UMR 5505, University of Toulouse, Toulouse, France

villain.edouard@gmail.com, {herwig.wendt, basarab, kouame}@irit.fr

## ABSTRACT

Tissue characterization based on ultrasound (US) images is an extensively explored research field. Most of the existing techniques are focused on the estimation of statistical or acoustic parameters from the backscattered radio-frequency signals, thus complementing the visual inspection of the conventional B-mode images. Additionally, a few studies show the interest of analyzing the fractal or multifractal behavior of human tissues, in particular of tumors. While biological experiments sustain such multifractal behaviors, the observations on US images are rather empirical. To our knowledge, there is no theoretical or practical study relating the fractal or multifractal parameters extracted from US images to those of the imaged tissues. The aim of this paper is to investigate how multifractal properties of a tissue correlate with the ones estimated from a simulated US image for the same tissue. To this end, an original simulation pipeline of multifractal tissues and their corresponding US images is proposed. Simulation results are compared to those in an *in vivo* experiment.

***Index Terms*—** Ultrasound imaging, multifractal analysis, tissue characterization

## 1. INTRODUCTION

Ultrasound (US) imaging is an extensively used imaging modality providing structural information about human tissues for number of clinical applications. To complement this structural information, several studies proposed to extract quantitative parameters from conventional B-mode images or raw radiofrequency (RF) data. These works are commonly addressed as tissue characterization or quantitative US. Most of them are based on the estimation of statistical or spectral-based parameters from image regions extracted from different tissues (e.g., [1]) or on the estimation of acoustic parameter maps such as the attenuation coefficient (e.g., [2]).

Based on biological studies showing that certain tissues such as tumors have a multifractal behavior in space and time (e.g., [3]), several existing works proposed to extract the fractal or multifractal signature of the tissues from US images and to use it for segmentation, characterization or classification purpose (e.g., [4–7]). However, to the best of our knowledge, no theoretical or practical analysis of the good agreement between the multifractal behavior of the tissues and the multifractal signature estimated from US images exists.

Starting from this observation, the aim of this paper is to propose an US simulation pipeline with available ground truth of tissue multifractal characteristics. From this tissue, we generate the corresponding US images. The proposed simulation allows the estimation of the multifractal spectrum from the tissue reflectivity map and from different US imaging modes (RF, envelope and B-mode) and to compare them with the ground truth. It thus gives an insight about the relevance of the estimated multifractal spectrum from US images. To obtain estimates for the multifractal spectra, use is made of the current state-of-the-art wavelet leader multifractal formalism [8, 9]. The results obtained with this model lead us to conclude that an important part of the multifractal characteristics of the simulated tissues is preserved in US (RF and envelope) images, but B-mode images bear no multifractal ressemblance with simulated tissues; similar findings are obtained in a thyroid *in vivo* experiment.

The remainder of this paper is organized as follows. Section 2 provides a brief summary on multifractal analysis. Section 3 details the proposed US simulation procedure. The simulation and experimental results are regrouped in Section 4, and conclusion and perspectives are presented in Section 5.

## 2. METHODOLOGY: MULTIFRACTAL ANALYSIS

### 2.1. Local regularity and multifractal spectrum

**Multifractal analysis.** Multifractal analysis is a modeling and analysis paradigm that enables texture in an image $F(\mathbf{x})$ to be characterized based on the *fluctuations* of its *local regularity index* $h(\mathbf{x}) > 0$, referred to as the Hölder exponent: the smaller (larger) $h(\mathbf{x})$, the rougher (smoother) $F(\mathbf{x})$ around location $\mathbf{x}$ [8, 9]. This caracterization is achieved by means of the so-named *multifractal spectrum* $\mathcal{D}(h)$, which provides a global description of the geometric repartition of $h(\mathbf{x})$ in space and is defined as the Haussdorf dimension of the sets of points $\mathbf{x}$ with identical exponent $h(\mathbf{x}) = h$. Theoretically, $\mathcal{D}(h)$ could be any function on the positive real axis taking values in $(0, 2) \cup \{-\infty\}$. Yet, it is in practice often sufficient to approximate it as a parabola, i.e.,

$$\mathcal{D}(h) \approx 2 + (h - c_1)^2/(2c_2), \tag{1}$$

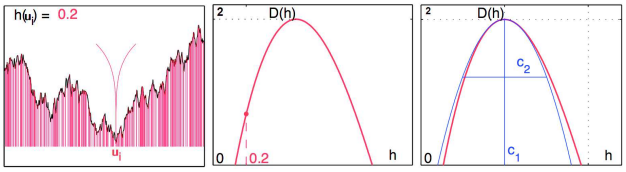


**Fig. 1**. **Multifractal spectrum.** $\mathcal{D}(h)$ (center) is defined as the fractal dimension of the iso-Hölder sets of the image (sketched in red for a 1D slice and $h = 0.2$, left) and can be approximated with a parabola with parameters $(c_1, c_2)$.

see Fig. 1 for an illustration. Practical multifractal analysis thus essentially consists in estimating the parameters in this approximation: $c_1$, which quantifies the average regularity of $F$ and accounts for self-similarity, whereas $c_2 \leq 0$ quantifies the regularity fluctuations and accounts for multifractality [9].

**Multifractal models.** Several works proposed the use of the seminal fractional Brownian motion (fBm), the only Gaussian self-similar model process with stationary increments, for modeling US images [6, 10, 11]. FBm is controlled by one single parameter, the self-similarity parameter $H$, and has regularity $h(\mathbf{x}) = H$ everywhere, hence $c_1 = H$, $c_2 = 0$, and $\mathcal{D}(h) = \delta(h - H)$. Yet, $c_2$ was observed to be strictly negative for US images, $c_2 < 0$ [7, 12]. This calls for the use of multifractal models that are more flexible to account for the non Gaussian and complex, intermittent regularity fluctuations observed in *in vivo* data. For further details about multifractal models, see, e.g., [8] and references therein.

### 2.2. Estimation of the multifractal spectrum

**Wavelet leaders.** The current state-of-the-art procedure for estimating $\mathcal{D}(h)$ relies on the *wavelet leaders* of discrete wavelet transform (DWT) coefficients and will be used here. The DWT coefficients of $F$ are defined as inner products $d_F^{(m)}(j, \boldsymbol{k}) = \langle F, \psi_{j,\boldsymbol{k}}^{(m)} \rangle$, $m = 0, \ldots, 3$ with an (L1-normalized) orthonormal basis of 2D wavelets [13]. They can be defined as the dilated (to scale $2^j$) and translated (to position $\boldsymbol{k}2^j$) tensorial products $\psi^{(0)}(\mathbf{x}) = \phi(x_1)\phi(x_2)$, $\psi^{(1)}(\mathbf{x}) = \psi(x_1)\phi(x_2)$, $\psi^{(2)}(\mathbf{x}) = \phi(x_1)\psi(x_2)$, $\psi^{(3)}(\mathbf{x}) = \psi(x_1)\psi(x_2)$ of the scaling function $\phi(x)$ and mother wavelet $\psi(x)$ for a 1D multiresolution analysis, $\psi_{j,\boldsymbol{k}}^{(m)}(\mathbf{x}) \triangleq 2^{-j}\psi^{(m)}(2^{-j}\mathbf{x} - \boldsymbol{k})$. The wavelet leaders are then defined as the largest DWT coefficients, across all finer scales and within a small spatial neighborhood $3\lambda_{j,\boldsymbol{k}}$ [8]: $\ell(j, \boldsymbol{k}) = \sup_{m\in(1,2,3),\lambda'\subset 3\lambda_{j,\boldsymbol{k}}} |2^{j\gamma} d_F^{(m)}(\lambda')|$, where $\lambda_{j,\boldsymbol{k}}$ is the dyadic cube of side length $2^j$ centered at $\boldsymbol{k}2^j$, $3\lambda_{j,\boldsymbol{k}} = \bigcup_{n_1,n_2=\{-1,0,1\}} \lambda_{j,k_1+n_1,k_2+n_2}$ the union of this cube with its eight neighbors, and $\gamma > 0$ is a parameter that can be tuned to match minimum regularity conditions on $F$ and will not be further discussed here. For technical details, see, e.g., [8, 9].

**Multifractal formalism.** It is well documented that the empirical $q$-th order moments of wavelet leaders behave as power-laws with respect to analysis scales $2^j$ for multifractal processes, $\sum_k \ell(j, k)^q \sim 2^{j\zeta(q)}$ in the limit of fine scales. It can be shown that the so-termed *scaling exponents* $\zeta(q)$ characterizing these power laws are tied to the multifractal spectrum via a Legendre transform: $\mathcal{L}(h) = \inf_q(2 + qh - \zeta(q)) \geq \mathcal{D}(h)$. This theoretical link permits to define simple and robust estimators for multifractal parameters. In particular, the power-law behavior of $q$-th order moments can be rewritten in terms of the cumulants of order $p \geq 1$, $C_p(j) = \mathrm{Cum}_p(\ln \ell(j, k))$, of the log-leaders $\ln \ell(j, k)$: $C_p(j) = c_p^0 + c_p \ln 2^j$. This has classically lead to the estimation of $c_1$ and $c_2$ by linear regressions of the average and sample variance of $\ln \ell(j, k)$ as functions of $\ln 2^j$ [8]. Finally, it can be shown that the coefficients $c_1$ and $c_2$ in this relation are precisely the coefficients of the parabolic approximation for $\mathcal{D}(h)$ in (1).

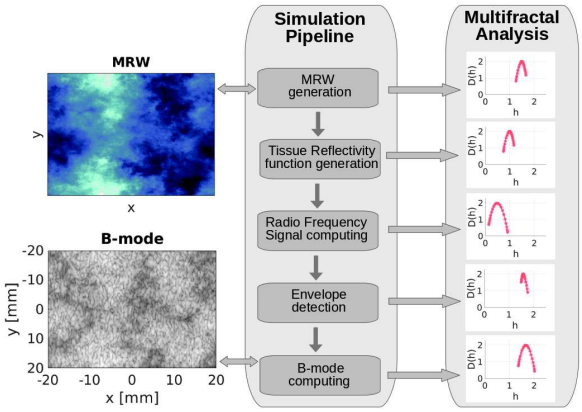


**Fig. 2**. **Schematic view of the proposed simulation pipeline:** i) generation of MRW image with prescribed multifractal properties; ii) TRF generation from randomly placed random scatterers with variance controlled by the MRW image; iii) convolution of the TRF with a system PSF to obtain RF image; iv) detection of the envelope of each RF signal; v) B-mode image obtained by log-compression; multifractal analysis is conducted at each level of the simulation pipeline.

## 3. US IMAGE SIMULATION PIPELINE

The proposed US simulation aims at investigating the relationship between the multifractal parameters of a tissue and the ones extracted from the resulting simulated image. Thus, the simulation pipeline follows the standard strategy used in US literature, but use is made of a tissue reflectivity function that is computed from a synthetic image mimicking a tissue with known multifractal ground truth, and the multifractal spectrum is estimated independently for each simulated image. The pipeline is illustrated in Fig. 2 and detailed next.

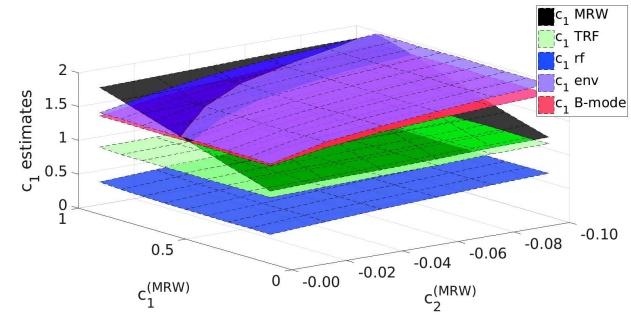


(a) $c_1$ estimation

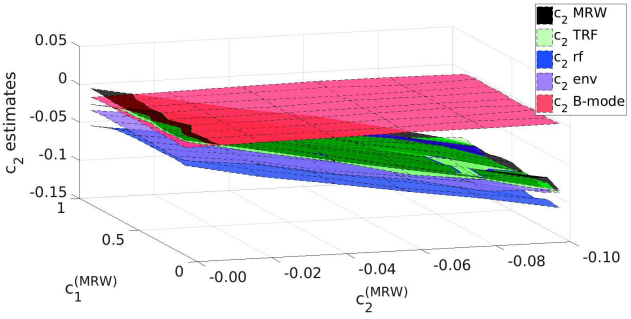


(b) $c_2$ estimation

**Fig. 3**. Average values of $c_1$ and $c_2$ estimates over 100 trials for several simulations with controlled multifractal properties.

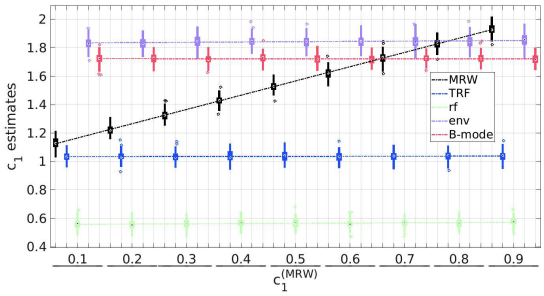


(a) $c_1$ estimation

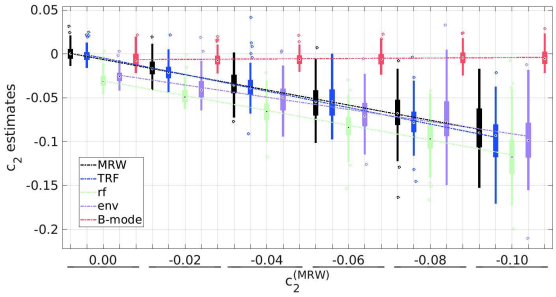


(b) $c_2$ estimation

**Fig. 4**. Average and standard deviation values for estimates of $c_1$ (for $c_2 = -0.06$ fixed) and $c_2$ (for $c_1 = 0.5$ fixed).

**i) Multifractal image.** The first step consists in generating an image with controlled multifractal properties. In this paper, this is achieved using multifractal random walk (MRW). MRW mimicks the multifractal properties of the celebrated Mandelbrot multiplicative cascades, and its multifractal spectrum is given by $\mathcal{D}(h) = 2 + (h - c_1)^2/(2c_2)$, see [14, 15] for technical details and definitions. It is chosen here for its ease of numerical synthesis and independent tuning of multifractal parameters. Synthesis procedures were implemented by ourselves as described in [16] and are available upon request.

**ii) Tissue reflectivity function (TRF).** The second step consists in generating a TRF, mimicking the scattering map, i.e., the presence of small particles (scatterers) in the human body that diffuse the propagating US waves. This TRF is computed from the MRW image as follows. First, scatterer positions are drawn at random from a uniform distribution in the field of view, in order to obtain US images with speckle characteristics close to those obtained in practical situations (see, e.g., scatterer map generation examples available within Field II simulator [17]). Then each scatterer is assigned a random amplitude, drawn from a zero mean Gaussian distribution with variance prescribed by the value of the MRW image pixel closest to its position. Finally, the scatterer map is interpolated on a rectangular grid, yielding a regularly sampled TRF enabling fast processing for the remaining simulation steps.

**iii) RF signal.** Next, the TRF is convolved with a realistic point spread function generated with Field II simulator [17], resulting into an RF image.

**iv) Envelope.** The RF image is further axially demodulated, resulting into an envelope image.

**v) B-mode image.** Finally, the RF image is log-compressed to obtain the standard B-mode image used in clinical routine.

An example of an MRW image and the resulting final B-mode image is shown in Fig. 2 (left).

## 4. RESULTS

### 4.1. Simulation results

Collections of MRW images with various multifractal parameters were simulated as described above. The value for the self-similarity parameter was set to $c_1 \in (0.1, 0.2, \ldots, 0.9)$, and for the multifractality parameter to $c_2 \in (-0.1, -0.08, \ldots, -0.02, 0)$, covering a large variety of realistic multifractal properties. For each combination $(c_1, c_2)$, 100 independent realizations of MRW of size $512 \times 512$ were synthesized and used in the simulation pipeline. The parameters $c_1$ and $c_2$ were estimated for MRW, TRF, RF, envelope and B-mode images, respectively, as detailed in Sec. 2, using Daubechies1 wavelets, $j_1 = 3$, $j_2 = 6$ and $\gamma = 2$; values reported for $c_1$ correspond to the primitive of the image. Results reported

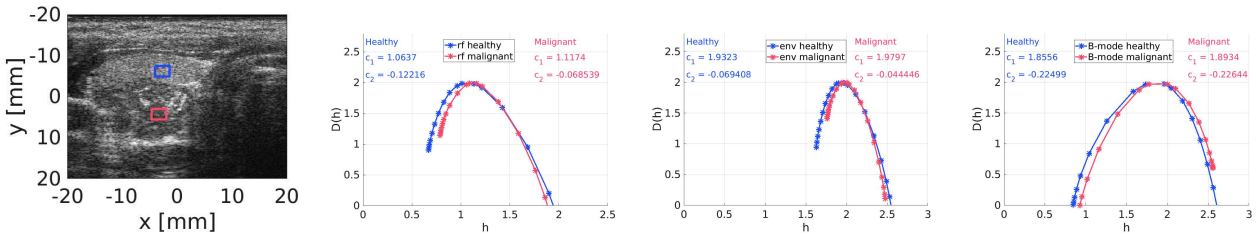


(a) (b) (c) (d)

**Fig. 5**. (a) B-mode image representing a thyroid with a malignant tumor, with blue (healthy tissue) and red (tumor) rectangles highlighting the analysed patches. (b-d) Multifractal spectra estimated from the respective RF, envelope and B-mode images.

below correspond to averages and standard deviations of estimates computed over independent realizations.

Fig. 3 plots average estimates for the self-similar parameter $c_1$ (top) and the multifractal parameter $c_2$ (bottom) obtained for MRW, TRF, RF, envelope and B-mode images, respectively, as a function of the values for $(c_1, c_2)$ prescribed for MRW. Estimations for MRW perfectly match the prescribed values, confirming the accuracy of the wavelet leader multifractal formalism [8]. As far as the simulated TRF and US images are concerned, Fig. 3 yields the following conclusions: For the B-mode image, neither $c_1$ nor $c_2$ estimates reveal changes in the multifractal properties of the MRW tissue model. For the TRF, RF and envelope images, the values estimated for the parameter $c_1$ capturing self-similarity is also insensitive to changes in the value that is prescribed for MRW. However, the estimated values for the parameter $c_2$ that measures *multifractality* strongly correlate with those prescribed for MRW.

Fig. 4 proposes a more quantitative analysis and plots the average and standard deviation values for $c_1$ (with constant $c_2 = -0.06$) and for $c_2$ (with constant $c_1 = 0.5$). The results confirm that the estimates for the multifractality parameter $c_2$ for the simulated TRF, RF and envelope images strongly correlate with the values prescribed for $c_2$. In other words, these images enable us to measure the multifractality of the synthetic tissue. This is not the case for the B-mode image, for which $c_2 \approx 0$. The results also show that the estimates for $c_1$ for any (TRF, RF, envelope and B-mode) simulated image are not coherent with the values for $c_1$ prescribed for the MRW underlying the simulation. One potential explanation for this observation could be that the independent random amplitudes of the scatterers in the TRF generation process bury the self-similarity $c_1$ of MRW.

### 4.2. Illustration for experimental data

We complement the simulation study with a result on an *in vivo* image acquired from a patient with a malignant thyroid tumor. Multifractal spectra were estimated for two image patches extracted from the tumor and the healthy thyroid tissue, respectively. To match the simulation, the patches were interpolated to images of size $512 \times 512$, with isotropic axial and lateral resolution of $\approx 6.5\mu m$. The B-mode image and these two patches are shown in Fig. 5(a). In this experiment, only the US modes (RF, envelope and B-mode) were available. Thus, three pairs (healthy vs. tumor) of multifractal spectra were estimated and are plotted in Fig. 5(c-d). We observe that the spectra estimated from the B-mode image are not highlighting any difference between the two tissues. However, the spectra estimated on RF and envelope images have different shapes for the healthy and pathological tissues. These different shapes are reflected by different values $c_2 < 0$, which is precisely the parameter that was observed to correlate with the multifractal properties of tissues in the above simulations. These differences could hence indicate a change in multifractality for the *tissues*. The position of the modes of the spectra, quantified by $c_1$, are observed to coincide - hence to be not discriminative - for the US images for both tissues, in coherency with the above simulation results.

## 5. CONCLUSION AND PERSPECTIVES

Multifractal analysis for US images aims at providing additional, quantitative information about the human tissues and has proven useful in classification or tissue characterization tasks. This work studied the relevance and interpretability of the estimated multifractal properties with respect to those of the tissues themselves through a simulation case. Its main originality comes from the simulation of US data from images with available multifractal ground truth, enabling the comparison of multifractal parameters estimated for US image with those of the multifractal ground truth, and assessing their correlation. In this model we observed that (i) while self-similar properties can be buried, the truly multifractal behavior is preserved in US images compared to the simulated tissues and (ii) B-mode images bear no multifractal ressemblance with simulated tissues. Results on real-world US images of tissue lead to similar conclusions. Our study opens several perspectives including a theoretical analysis of the simulation results, evaluation of the impact of deconvolution algorithms giving access to the TRF, and the analysis of *in vivo* data sets.

## 6. REFERENCES


[1] M. L. Oelze and J. Mamou, "Review of quantitative ultrasound: Envelope statistics and backscatter coefficient imaging and contributions to diagnostic ultrasound," *IEEE Transactions on Ultrasonics, Ferroelectrics, and Frequency Control*, vol. 63, no. 2, pp. 336–351, Feb 2016.

[2] A. L. Coila and R. Lavarello, "Regularized spectral log difference technique for ultrasonic attenuation imaging," *IEEE Transactions on Ultrasonics, Ferroelectrics, and Frequency Control*, vol. 65, no. 3, pp. 378–389, March 2018.

[3] M. Molski and J. Konarski, "Tumor growth in the space-time with temporal fractal dimension," *Chaos, Solitons & Fractals*, vol. 36, no. 4, pp. 811 – 818, 2008.

[4] M. A. Mohammed, B. Al-Khateeb, A. N. Rashid, D. A. Ibrahim, M. K. A. Ghani, and S. A. Mostafa, "Neural network and multi-fractal dimension features for breast cancer classification from ultrasound images," *Computers & Electrical Engineering*, vol. 70, pp. 871 – 882, 2018.

[5] R. Zhou, Y. Luo, A. Fenster, J. D. Spence, and M. Ding, "Fractal dimension based carotid plaque characterization from three-dimensional ultrasound images," *Medical & Biological Engineering & Computing*, Jul 2018.

[6] O. S. Al-Kadi, "Fractals for biomedical texture analysis," in *Biomedical Texture Analysis*, A. Depeursinge, O. S. Al-Kadi, and J. Mitchell, Eds. Academic Press, 2017, pp. 131 – 161.

[7] M. Djeddi, A. Ouahabi, H. Batatia, A. Basarab, and D. Kouamé, "Discrete wavelet for multifractal texture classification: application to medical ultrasound imaging," in *2010 IEEE International Conference on Image Processing*, Sept 2010, pp. 637–640.

[8] H. Wendt, P. Abry, and S. Jaffard, "Bootstrap for empirical multifractal analysis," *IEEE Signal Processing Magazine*, vol. 24, no. 4, pp. 38–48, 2007.

[9] H. Wendt, S. G. Roux, P. Abry, and S. Jaffard, "Wavelet leaders and bootstrap for multifractal analysis of images," *Signal Processing*, vol. 89, no. 6, pp. 1100–1114, 2009.

[10] D.-R. Chen, R.-F. Chang, C.-J. Chen, M.-F. Ho, S.-J. Kuo, S.-T. Chen, S.-J. Hung, and W. K. Moon, "Classification of breast ultrasound images using fractal feature," *Clinical imaging*, vol. 29, no. 4, pp. 235–245, 2005.

[11] W.-L. Lee, Y.-C. Chen, and K.-S. Hsieh, "Ultrasonic liver tissues classification by fractal feature vector based on m-band wavelet transform," *IEEE Transactions on Medical Imaging*, vol. 22, no. 3, pp. 382–392, 2003.

[12] R. Lopes and N. Betrouni, "Fractal and multifractal analysis: A review," *Medical Image analyis*, vol. 13: 634-49, 2009.

[13] S. Mallat, *A Wavelet Tour of Signal Processing*, 3rd ed. Academic Press, 2008.

[14] E. Bacry, J. Delour, and J.-F. Muzy, "Multifractal random walk," *Phys. Rev. E*, vol. 64: 026103, 2001.

[15] P. Abry, P. Chainais, L. Coutin, and V. Pipiras, "Multifractal random walks as fractional wiener integrals," *IEEE Transactions on Information Theory*, vol. 55, pp. 3825–3846, 2009.

[16] L. Chevillard, R. Robert, and V. Vargas, "A stochastic representation of the local structure of turbulence," *Europhysics Letters*, vol. 89, p. 54002, March 2010.

[17] J. Jensen, "Simulation of advanced ultrasound systems using Field II," in *IEEE International Symposium on Biomedical Imaging: Nano to Macro, 2004*, April 2004, pp. 636–639 Vol. 1.